

University of Wollongong

Research Online

Australian Institute for Innovative Materials -
Papers

Australian Institute for Innovative Materials

1-1-2018

Graphitic Carbon Nanocage as a Stable and High Power Anode for Potassium-Ion Batteries

Bin Cao

University of Wollongong, Beijing University of Chemical Technology

Qing Zhang

University of Wollongong, qz964@uowmail.edu.au

Huan Liu

Beijing University of Chemical Technology

Bin Xu

Beijing University of Chemical Technology

Shilin Zhang

University of Wollongong, sz384@uowmail.edu.au

See next page for additional authors

Follow this and additional works at: <https://ro.uow.edu.au/aiimpapers>



Part of the [Engineering Commons](#), and the [Physical Sciences and Mathematics Commons](#)

Recommended Citation

Cao, Bin; Zhang, Qing; Liu, Huan; Xu, Bin; Zhang, Shilin; Zhou, Tengfei; Mao, Jianfeng; Pang, Wei Kong; Guo, Zaiping; Li, Ang; Zhou, Jisheng; Chen, Xiaohong; and Song, Huaihe, "Graphitic Carbon Nanocage as a Stable and High Power Anode for Potassium-Ion Batteries" (2018). *Australian Institute for Innovative Materials - Papers*. 3281.

<https://ro.uow.edu.au/aiimpapers/3281>

Research Online is the open access institutional repository for the University of Wollongong. For further information contact the UOW Library: research-pubs@uow.edu.au

Graphitic Carbon Nanocage as a Stable and High Power Anode for Potassium-Ion Batteries

Abstract

As an emerging electrochemical energy storage device, potassium-ion batteries (PIBs) have drawn growing interest due to the resource-abundance and low cost of potassium. Graphite-based materials, as the most common anodes for commercial Li-ion batteries, have a very low capacity when used as an anode for Na-ion batteries, but they show reasonable capacities as anodes for PIBs. The practical application of graphitic materials in PIBs suffers from poor cyclability, however, due to the large interlayer expansion/shrinkage caused by the intercalation/deintercalation of potassium ions. Here, a highly graphitic carbon nanocage (CNC) is reported as a PIBs anode, which exhibits excellent cyclability and superior depotassiation capacity of 175 mAh g⁻¹ at 35 °C. The potassium storage mechanism in CNC is revealed by cyclic voltammetry as due to redox reactions (intercalation/deintercalation) and double-layer capacitance (surface adsorption/desorption). The present results give new insights into structural design for graphitic anode materials in PIBs and understanding the double-layer capacitance effect in alkali metal ion batteries.

Disciplines

Engineering | Physical Sciences and Mathematics

Publication Details

Cao, B., Zhang, Q., Liu, H., Xu, B., Zhang, S., Zhou, T., Mao, J., Pang, W., Guo, Z., Li, A., Zhou, J., Chen, X. & Song, H. (2018). Graphitic Carbon Nanocage as a Stable and High Power Anode for Potassium-Ion Batteries. *Advanced Energy Materials*, 8 (25), 1801149-1-1801149-7.

Authors

Bin Cao, Qing Zhang, Huan Liu, Bin Xu, Shilin Zhang, Tengfei Zhou, Jianfeng Mao, Wei Kong Pang, Zaiping Guo, Ang Li, Jisheng Zhou, Xiaohong Chen, and Huaihe Song

DOI: 10.1002/((please add manuscript number))

Article type: Communication

Graphitic carbon nanocage as a stable and high power anode for potassium-ion batteries

Bin Cao, Qing Zhang, Huan Liu, Bin Xu, Shilin Zhang, Tengfei Zhou, Jianfeng Mao, Wei Kong Pang, Zaiping Guo,* Ang Li, Jisheng Zhou, Xiaohong Chen, Huaihe Song**

B. Cao, Dr. A. Li, Prof. J. Zhou, Prof. X. Chen, Prof H. Song
State Key Laboratory of Chemical Resource Engineering, Beijing Key Laboratory of Electrochemical Process and Technology for Materials, Beijing University of Chemical Technology, Beijing 100029, China
E-mail: songhh@mail.buct.edu.cn

Dr. H. Liu, Prof. B. Xu
State Key Laboratory of Organic-Inorganic Composites, Beijing Key Laboratory of Electrochemical Process and Technology for Materials, Beijing University of Chemical Technology, Beijing 100029, China
E-mail: binxumail@163.com

B. Cao, Q. Zhang, S. Zhang, Dr. T. Zhou, Dr. J. Mao, Dr. W. K. Pang, Prof. Z. Guo
Institute for Superconducting and Electronic Materials, School of Mechanical, Materials and Mechatronics Engineering, University of Wollongong, North Wollongong, NSW 2500, Australia
E-mail: zguo@uow.edu.au

Keywords: Potassium-ion batteries, anode, carbon nanocage, cyclability, rate capability

Abstract: As an emerging electrochemical energy storage device, potassium-ion batteries (PIBs) have drawn growing interest due to the resource-abundance and low cost of potassium. Graphite-based materials, as the most common anodes for commercial Li-ion batteries, have a very low capacity when used as anode for Na-ion batteries, but they show reasonable capacities as anodes for PIBs. The practical application of graphitic materials in PIBs suffers from poor cyclability, however, due to the large interlayer expansion/shrinkage caused by the intercalation/de-intercalation of potassium ions. Here, a highly graphitic carbon nanocage (CNC) is reported as a PIBs anode, which exhibits excellent cyclability and superior depotassiation capacity of 175 mAh g⁻¹ at 35 °C. The potassium storage mechanism in CNC was revealed by cyclic voltammetry as due to redox reactions (intercalation/de-intercalation) and double-layer capacitance (surface adsorption/desorption). The present results give new insights

into structural design for graphitic anode materials in PIBs and understanding the double-layer capacitance effect in alkali metal ion batteries.

Lithium-ion batteries (LIBs) have been widely used in portable electronic devices and are regarded as the most promising candidates for electric vehicles due to their high energy and power densities.^[1] Since large-scale electrical energy storage systems are critical for utilizing intermittent renewable energy, in the foreseeable future, the high cost and the limited nature of lithium resources would hinder further application of LIBs in this field.^[2,3] Therefore, secondary metal-ion batteries based on low-cost and resource abundant elements (such as Na,^[4-6] Mg,^[7] Al^[8] and K^[9-11]) are being widely considered. Among these emerging battery technologies, potassium-ions batteries (PIBs) have great advantages as an ideal alternative for LIBs because potassium not only is a low-cost, non-toxic and resource-abundant element (2.4 wt.% potassium in the Earth's crust), but also has a low redox potential of -2.93 V vs. standard hydrogen electrode (SHE) as the K^+/K couple, resulting in a high working voltage and high energy density for PIBs with low cost.

To date, alloy-based materials,^[12-16] transition-metal oxides/sulfides,^[17-19] and MXene-based materials^[20-22] have been reported as anode materials for PIBs. Carbon-based anode materials,^[23-37] however, are regarded as the most promising ones for large-scale applications. As one advantage for PIBs, graphite, the current commercial anode material for LIBs, can be used as anode for PIBs.^[23a, 25] Accordingly, PIBs could be well suited to the existing LIB manufacturing technology due to their similar working mechanism and cell structure.^[38] Graphitic materials show amazing electrochemical activity when used as anode for PIBs, since their layered structure is available for K^+ intercalation to form the stage-one K-graphite intercalation compound (KC_8) with the theoretical capacity of 279 mAh g^{-1} .^[23a] Moreover, the graphitic materials have a long and stable K^+ intercalation/de-intercalation plateau above 0.1 V vs. K^+/K . This low plateau potential not only is suitable for a high working voltage and thus

high energy density when coupled with cathode materials,^[39] but also avoids the formation of potassium dendrites and the related safety concerns. Nevertheless, the full potassiation of graphite with almost 60% incremental expansion in the interlayer distance would lead to irreversible structural damage due to the larger K^+ radius (1.38 Å, almost 1.82 times larger than Li^+). Therefore, potassiation/depotassiation of graphite is not highly reversible, even under charge/discharge at low current density. With few reports on graphitic carbon anodes for PIBs,^[23-25] this issue is still not effectively solved. Therefore, the main problem for graphite as an anode material of PIBs is the severe structural degradation during cycling. Accordingly, designing a highly stable structure to accommodate the expansion in interlayer distance during charge/discharge is urgent for application of graphitic materials in PIBs.

In this study, we propose a highly graphitic carbon nanocage (CNC) to meet the requirements on anode materials for PIBs. The cage-like structure could effectively reduce anisotropy due to the concentric arrangement of carbon layers and thus avoid interlayer slipping to ensure structural integrity. Accordingly, the hollow cage-like structure could effectively accommodate the strain relaxation during K^+ intercalation/de-intercalation and thus improve the cyclability. Moreover, the interconnected network structure of CNC is a three-dimensional (3D) electrically conducting network that permits fast electron transfer among the different carbon nanocages, thus achieving better electrochemical kinetics to ensure excellent rate performance. Based on the above, CNC exhibits excellent cyclability and a superior depotassiation capacity of 175 mAh g⁻¹ with high capacity retention of 79% at 35 °C. In addition, the cyclic voltammetry analysis has revealed the hybrid potassium storage mechanism in CNC, i.e. redox reactions (intercalation/de-intercalation) and double-layer capacitance (surface adsorption/desorption). The present results give new insights into structural design for graphitic anode materials with stable cyclability in PIBs and understanding the hybrid potassium storage mechanism.

The CNC were prepared by high temperature treatment of Ketjen carbon black (EC300J) at 2800°C under Ar atmosphere (**Figure S1** in the Supporting Information). Since Ketjen carbon black is a commercially available material and the high-temperature treatment of carbonaceous materials is a mature technology, the production of CNC could be easily scaled up. The CNC has the appearance of a string of grapes with interconnected structure in 3D space (**Figure 1a**), and the integrated structure can be further proved by the high resolution transmission electron microscope (HRTEM) image (**Figure 1b**). In addition, the CNC has a uniform hollow cage-like morphology (**Figure 1c**) with an average particle diameter of about 50 nm and a shell thickness of ~ 5 nm. The interconnected structure could permit fast electron transfer among different nanocages (illustrated schematically in **Figure 1d**), and the hollow nanocage morphology with thin shells could effectively reduce the ion diffusion length in solid phase, thus achieving better electrochemical kinetics to ensure excellent rate performance. In the X-ray diffraction (XRD) patterns (**Figure 1e**), the sharp (002) peak indicates the highly graphitic layered structure of CNC, which is critical to ensure its typical graphite-like electrochemical behavior with a low potassium storage potential for PIBs. The Raman spectrum of CNC (**Figure 1f**) shows a strong G band (1585 cm⁻¹, graphitic structure) and D band (1360 cm⁻¹, defective structure). The integrated intensity ratio of the G band to the D band (I_G/I_D) is as high as 3.96, confirming the highly ordered graphitic structure of CNC, which corresponds to the XRD and HRTEM results. Furthermore, the appearance of the D band reveals the existence of defective sites on the surface of nanocage, suggesting an imperfectly closed cage-like structure for the CNC. Unlike the edge sites in graphite-based materials with open layered structure, those surface defective sites are active sites for ion intercalation/de-intercalation.^[40] As a reference sample, mesophase graphite (MG) was prepared in our laboratory by polycondensation from coal tar pitch and graphitization at 2800°C. This widely applied commercial LIBs anode material with high cycling stability has a highly graphitic nature (XRD pattern and Raman spectrum in **Figure 1e** and **f**, respectively) with an open-layered structure (**Figure S2**).

The potassium intercalation/de-intercalation behavior of CNC was investigated by cyclic voltammetry (CV) and galvanostatic charge-discharge. As shown in **Figure 2a** (CV curves at scan rate of 0.1 mV s^{-1}), potassium ion intercalation/de-intercalation in CNC can be clearly observed by the presence of two pairs of redox peaks between 0 and 0.6 V vs. K^+/K , which correspond to the phase transformation phenomenon of K-graphite intercalation compounds (K-GICs) from a dilute stage to a high stage (Stage 1, KC_8) and their backward transformation.^[23a, 24] A strong reduction peak around 0.7 V can be observed only in the first scan, which is attributed to the formation of solid electrolyte interphase (SEI) due to the decomposition of electrolyte.^[23a] In the following scans, the CV curves are almost overlapping, indicating the excellent electrochemical reversibility of CNC. In the high potential region (0.6-3.0 V vs. K^+/K), the well separated cathodic and anodic segments with rectangular shape in the CV curves of CNC electrode imply significant capacitive potassium storage behavior in comparison with the CV curve of MG electrode (**Figure S3a**). Voltage profiles of CNC and MG electrodes at the current density of 0.2 C ($1 \text{ C} = 279 \text{ mA g}^{-1}$) are shown in **Figure 2b** and **Figure S3b**, respectively. The long and stable voltage plateaus above 0.1 V vs. K^+/K help to avoid the formation of potassium dendrites and allow a high working voltage when coupled with a cathode in the full cell system.^[9, 10] From **Figure 2b**, several small plateaus corresponded to the different stage phase transformations can be well distinguished, which are consistent with the CV results. In the initial charge-discharge, a large irreversible capacity can be observed, corresponding to the formation of the SEI due to the high surface area of CNC. During the following 50 charge-discharge cycles, the overlapping voltage profiles suggest the excellent cyclability of CNC. In comparison with CNC, the separated voltage profiles of MG (**Figure S3b**) indicate fast capacity fading. Moreover, the small voltage hysteresis (**Figure S3c**) between the charge and discharge curves of CNC also confirms the far better electrochemical kinetics than that of MG. This improvement of CNC is likely to be due to the large specific surface area ($102.7 \text{ m}^2 \text{ g}^{-1}$), which provides higher electrochemical activity, and the thin shells of graphitic

nanocages, which reduce the ion diffusion distance in the solid phase. The cycling performances of CNC and MG at 0.2 C are shown in **Figure 2c**. The CNC delivers an initial reversible capacity of 212 mAh g⁻¹ with a Coulombic efficiency of 40%. The reversible capacity of CNC is lower than the theoretical capacity of KC₈, which is ascribed to the presence of crystal defects in CNC, such as turbostratic structure. Since the stage 1 intercalation compounds (such as KC₈ and LiC₆) prefer adjacent carbon layers with “AAAA” stacking arrangement^[23b,c], carbon layers with turbostratic disorder unable shift into the “AAAA” stacking arrangement to form stage 1 intercalation compound^[23d] thus resulting lower capacity of CNC than the theoretical capacity. The low initial Coulombic efficiency of CNC is ascribed to its large surface area, which consumes more electrolyte for the formation of SEI and can potentially be improved by additives in the electrolyte or using pre-potassiation technology.^[41] After 100 cycles, CNC still has a reversible capacity of 195 mAh g⁻¹ with a high capacity retention of 92%. After 140 cycles, further cycles can be achieved by replacing potassium metal and adding new electrolyte to the cell due to the potassium metal with high chemical activity consuming limited amount of electrolyte (shown in **Figure S4** and see more detailed discussion in Supporting Information).^[9] Although MG has a higher initial reversible capacity of 248 mAh g⁻¹ at 0.2 C, its reversible capacity decreases gradually with cycling. After 50 cycles, only 62% of the initial capacity can be maintained. The fast capacity fading in MG electrode may be ascribed to structural degradation induced by the large expansion in interlayer distance.

In order to reveal the different cyclability of CNC and MG electrodes after 100 cycles at 0.2 C, the electrodes were characterized by HRTEM. As the HRTEM images shown in **Figure 2d**, the interconnected cage structure of CNC still can be clearly observed, which is essential to ensure stable cyclability. The well-dispersed C, K, F, S, and O elements (**Figure 2e**) that have come from SEI components revealed the stable nature of the electrode/electrolyte interface during cycling. Moreover, the interlayer spacing in the original CNC and the CNC after 1 cycle were evaluated by selected area electron diffraction (SAED) in **Figure S5**. The results indicated

that the interlayer spacing in CNC was increased to 3.53 Å from 3.46 Å, suggesting that the few-layer graphitic shell structure can be expanded. After 100 cycles, the interlayer spacing in CNC was 3.54 Å, which is very similar to that of CNC after 1 cycle, demonstrating that the high structure stability of CNC, and the few-layer graphitic shell can reversibly expand/shrink due to potassium intercalation/de-intercalation. By comparison, the MG was exfoliated to carbon nanosheets dispersed in amorphous SEI (**Figure 2f**), indicating severe structural degradation owing to large interlayer change during potassiation/depotassiation. It is well known that the structural degradation would also consume electrolyte and increase the internal resistance, thus leading to cell failure. For reviewing the interfacial features of the carbon electrodes in different cycles and avoiding interference from potassium metal, electrochemical impedance spectroscopy (EIS) was carried out on symmetric cells (see more discussion of symmetric cell EIS in the Supporting Information) after different cycles (**Figure S6**). The semicircle in Nyquist plots of fresh cells reflects the intrinsic interface impedance between the carbon particles and the electrolyte, which is related to the electronic resistance of the electrode and the ion adsorption process on surfaces. After cycling, the semicircles became depressed and large, indicating a new interface state due to the formation of the passivated layer. For CNC electrodes (**Figure 2g**), the diameter of the semicircle increased gradually from the 1st cycle to the 10th cycle, while the Coulombic efficiency increased rapidly to 95% from 40% (**Figure 2c**), and then remained stable, even after the 30th cycle, suggesting that the SEI layer is stable after initial few cycles of activation. For MG electrodes, however, the diameter of the semicircle keeps growing as cycling continues, indicating that structural degradation has induced the repeated growth of SEI. Thus, we can conclude that there is no significant structural degradation of CNC during cycling, which is consistent with the HRTEM observations (**Figure 2d**). It is well known that a stable electrode/electrolyte interface is critical for stable electrochemical performance. Since the outer surface of CNC is composed of carbon basal planes, there is no doubt that the formation of a stable electrode/electrolyte interface can be ascribed to its unique

cage-like structure. As mentioned above, the excellent cyclability of CNC should be attributed to its cage-like structure, because the cage-like structure could effectively reduce the anisotropy due to the concentric arrangement of carbon layers and thus avoid interlayer slipping to ensure structural integrity. The cage-like structure possesses high chemical and structural stability, as it cannot be exfoliated by Hummers' method under rigorous conditions.^[42] Moreover, the cage-like structure is also a hollow structure. Since hollow structure has been demonstrated to be an attractive structure with excellent electrochemical performance in LIB/sodium ion battery (SIB) electrode materials,^[43-45] the unique hollow structure could effectively accommodate strain relaxation during potassium ion intercalation/de-intercalation and thus help to maintain the structural integrity to alleviate capacity fading.^[46] The poor cycling performance of MG is ascribed to its open-layered structure, which could not endure the large interlayer changes during potassiation/depotassiation. The structural variations of CNC and MG during potassium storage are schematically illustrated in **Figure 2i**.

The rate capability between CNC and MG was also compared, as shown in **Figure S7**. CNC has a reversible capacity of 137, 99, 71, and 56 mAh g⁻¹ at current rates of 0.5 C, 1 C, 2 C, and 3 C, respectively. Even at the high current density of 5 C, the CNC can still deliver a reversible capacity of 40 mAh g⁻¹. Among the reported graphitic materials,^[23a, 24, 26] CNC has the superior rate performance. In contrast, the capacity of MG quickly dropped to 100 mAh g⁻¹ at 0.5 C and only 30 mAh g⁻¹ at 1 C. Although CNC exhibits much superior rate capability to MG, the capacity drop of CNC at high current rates seems too fast, which is ascribed to the large polarization and impedance in the potassium half-cell (**Figure S8**) because potassium metal may not be a good reference electrode (see more comments in the Supporting Information).^[10] To further examine the depotassiation capability of CNC and avoid the influence of polarization on potassiation, CNC electrode was potassiated at 0.1 C and depotassiated at different rates. As shown in **Figure 3a**, CNC can present a large reversible capacity of 175 mAh g⁻¹ at an ultrahigh rate of 35 C, i.e. the capacity retention is as high as 79% of that at 0.1 C (221.5 mAh g⁻¹). These

results indicate that CNC has outstanding high-rate depotassiation capability. As summarized in **Table S1**, a stable plateau with a capacity contribution of 75% is rarely reported at such a high rate of 35 C. After high rate depotassiation, the CNC electrode was taken out from the cell and characterized by HRTEM. It is clearly observed that CNC still had an interconnected cage structure with no exfoliation (**Figure 3c**), indicating that there was no structural degradation during high rate depotassiation.

The electrochemical behavior and kinetics of CNC were analyzed by CV techniques to gain further insight. As mentioned above, the CV curves of CNC show two different types of electrochemical behaviors in the low and high potential ranges. In the low potential range, the redox peaks dominated region (**Figure S9a**), indicating the typical faradic process, is attributed to the K^+ intercalation/de-intercalation reaction. For the high potential range (**Figure S9a** and **b**), the rectangle-shaped region is attributed to the double-layer capacitive behavior, as CNC has a well-developed surface area. This phenomenon has been observed and accepted in both lithium storage (**Figure S9c** and **d**) and sodium storage,^[47-51] proving the ubiquity of double-layer capacitance in electrochemical energy storage systems with electrode materials that have a high specific surface area. The CV curves for CNC/K half-cells at various scan rates from 0.01 to 0.5 $mV\ s^{-1}$ (**Figure 4a**) show similar shapes with redox peaks in the low potential region and a rectangular shape in the high potential region, indicating intercalation and double-layer capacitance dominated behaviors, respectively.^[52] The capacitive effects were analyzed by the power law relationship between the measured current (i) and the sweep rate (v) according to the following equation:

$$i = av^b, \quad (\text{Equation 1})$$

where the b -value can be determined from the slope of the plot of $\log(i)$ vs. $\log(v)$.^[52,53] For $b = 0.5$, the current is diffusion-controlled, indicating a faradaic intercalation process; moreover, $b = 1$ represents a capacitive response because the capacitive current is linearly proportional to the scan rate. As shown in **Figure 4b**, the b -values were plotted as a function of potential in the

cathodic scan. At potentials higher than 0.7 V, the b -values are in the range of 0.8-1.0, suggesting that the current is dominated by capacitive behavior. This result also corresponds with the rectangular shape in the CV curves within the high potential range (Figure 4a). In the low potential range of 0-0.5 V, the b -values are slightly higher than 0.5 within the range of 0.55-0.65. This result indicates that the response current due to double-layer capacitance is independent of the potential, although the current comes primarily from the K^+ intercalation in a faradaic intercalation dominated process. Therefore, capacitive behavior should exist throughout the reduction. The capacitive characteristics of CNC was also investigated in a CNC symmetric cell. As shown in Figure 4c, the CV curves show a typical rectangular shape even at an ultrahigh scan rate of 50 V s^{-1} , indicating the extraordinary power capability of CNC.^[54]

Since the response current from the double-layer capacitance is linearly proportional to the scan rate and exhibits rectangular shape in the CV curve,^[52] we assume that the capacitive current is not affected by the faradic current, so that the double-layer capacitance contribution in potassiation can be quantified based on the current response at high potential. A typical separation of the double-layer capacitance contribution is shown in Figure 4d. Note that the capacitive contribution was considered only in the cathodic process (K^+ intercalation) because the current baseline in the anodic scan is difficult to distinguish. The ratios of double-layer capacitance to the total charge are shown in Figure 4e, the quantitative results indicate that the double-layer capacitance contribution is 12.8% at 0.01 mV s^{-1} , which increases gradually with the scan rate and reaches a value of 22.1% at 0.5 mV s^{-1} . Furthermore, the capacity retention of intercalation reactions drops quickly with scan rate. The capacity retention of double-layer capacitance decreases slowly, however, and is always higher than that of intercalation reactions at the same scan rates, because a capacitor has a better rate durability than a battery. Therefore, we may conclude that the double-layer capacitance effect should not be neglected due to its high power capability.

The diffusion coefficients of CNC and MG were evaluated from the galvanostatic intermittent titration technique (GITT) profiles (**Figure S10** and **S11**) by Fick's second law using **Equation S1**.^[27] In potassiation, the diffusion coefficients decrease slowly below 0.25 V and then drop quickly, suggesting that the formation of a high stage intercalation compound might be the kinetics limited step. For depotassiation, the diffusion coefficients with relatively higher values throughout the process reveal the excellent depotassiation capability of CNC, which is consistent with previous electrochemical tests. Moreover, CNC shows lower over-potential and higher diffusion coefficients than MG in both potassiation and depotassiation, suggesting better electrochemical kinetics for CNC than that for MG. The potassium storage mechanism in CNC consists of potassium intercalation with high energy density and surface capacitive adsorption with high power density, which is briefly shown in **Figure 4f**.

In conclusion, CNC exhibits excellent cyclability and a superior depotassiation capacity of 175 mAh g⁻¹ with high capacity retention of 79% at 35 °C. The excellent cyclability and depotassiation capability of CNC are attributed to its unique interconnected cage structure as well as its hybrid potassium storage mechanism. First, the cage-like structure could effectively reduce anisotropy due to the concentric arrangement of carbon layers, and thus avoid interlayer slipping to ensure structural integrity. Moreover, the hollow structure could effectively accommodate strain relaxation during potassium ion intercalation/de-intercalation and thus help to maintain the structural integrity. It is well known that maintaining the structural integrity during electrochemical reactions is essential for maintaining stable electrochemical properties. Therefore, the ultra-stable cage-like structure is the basis for realizing stable electrochemical reactions. Second, the thin shell of CNC could effectively reduce the K⁺ diffusion distance in the solid phase, while the interconnected structure of CNC represents a 3D electrically conducting network that permits fast electron transfer among the different cages, thus achieving better electrochemical kinetics to ensure excellent rate performance. Last but not least, the highly graphitic structure of CNC is essential to ensure the low and stable K⁺ intercalation/de-

intercalation potential, which would be helpful for realizing a high working voltage in K-ion full cells. The hybrid potassium storage mechanism in CNC was revealed by cyclic voltammetry as due to redox reactions (intercalation/de-intercalation) and double-layer capacitance (surface adsorption/desorption). The quantified capacitive contributions indicate that the double-layer capacitance effect with high capacity retention is critical for achieving high power capability. As a non-negligible potassium storage behavior, the double-layer effect also plays an important role in realizing high power performance in CNC electrodes due to the nature of adsorption/desorption. In future research, the ratio between capacitance and intercalation, which offers a combined energy storage with redox reactions (chemical energy storage) and surface adsorption/desorption (physical energy storage), should be optimized to achieve a good balance between the energy density and power density.

Supporting Information

Supporting Information is available from the Wiley Online Library or from the author.

Acknowledgements

B.C. and Q.Z. contributed equally to this work. This work was supported by the National Natural Science Foundation of China (U1610252) and the National Key Research and Development Program of China (2017YFB0102204). Financial support provided by the Australian Research Council through DP170102406 is gratefully acknowledged. B.C. thanks the Graduate School of Beijing University of Chemical Technology for the financial support from the International Joint Graduate-Training Program. The authors acknowledge the support from Dr. Tania Silver for English editing of the manuscript.

Received: ((will be filled in by the editorial staff))

Revised: ((will be filled in by the editorial staff))

Published online: ((will be filled in by the editorial staff))

References

- [1] J. B. Goodenough, *Nat. Electron.* **2018**, 1, 204.
- [2] J. Tarascon, *Nat. Chem.* **2010**, 2, 510.
- [3] D. Larcher, J. Tarascon, *Nat. Chem.* **2014**, 7, 19.

- [4] N. Yabuuchi, K. Kubota, M. Dahbi, S. Komaba, *Chem. Rev.* **2014**, 114, 11636.
- [5] J. Mao, T. Zhou, Y. Zheng, H. Gao, H. K. Liu, Z. Guo, *J. Mater. Chem. A* **2018**, 6, 3284.
- [6] H. Liu, M. Jia, B. Cao, R. Chen, X. Lv, R. Tang, F. Wu, B. Xu, *J. Power Sources* **2016**, 319, 195.
- [7] Z. Zhang, Z. Cui, L. Qiao, J. Guan, H. Xu, X. Wang, P. Hu, H. Du, S. Li, X. Zhou, S. Dong, Z. Liu, G. Cui, L. Chen, *Adv. Energy Mater.* **2017**, 7, 1602055.
- [8] M. Lin, M. Gong, B. Lu, Y. Wu, D. Wang, M. Guan, M. Angell, C. Chen, J. Yang, B. Hwang, H. Dai, *Nature* **2015**, 520, 324.
- [9] X. Wu, D. P. Leonard, X. Ji, *Chem. Mater.* **2017**, 29, 5031.
- [10] A. Eftekhari, Z. Jian, X. Ji, *ACS Appl. Mater. Inter.* **2017**, 9, 4404.
- [11] J. C. Pramudita, D. Sehwat, D. Goonetilleke, N. Sharma, *Adv. Energy Mater.* **2017**, 7, 1602911.
- [12] W. Zhang, J. Mao, S. Li, Z. Chen, Z. Guo, *J. Am. Chem. Soc.* **2017**, 139, 3316.
- [13] Q. Zhang, J. Mao, W. K. Pang, T. Zheng, V. Sencadas, Y. Chen, Y. Liu, Z. Guo, *Adv. Energy Mater.* **2018**, 1703288.
- [14] K. Lei, C. Wang, L. Liu, Y. Luo, C. Mu, F. Li, J. Chen, *Angew. Chem. Int. Ed.* **2018**, [https://doi.org/ 10.1002/anie.201801389](https://doi.org/10.1002/anie.201801389).
- [15] K. Huang, Z. Xing, L. Wang, X. Wu, W. Zhao, X. Qi, H. Wang, Z. Ju, *J. Mater. Chem. A* **2018**, 6, 434.
- [16] I. Sultana, M. M. Rahman, Y. Chen, A. M. Glushenkov, *Adv. Funct. Mater.* **2018**, 28, 1703857.
- [17] H. Gao, T. Zhou, Y. Zheng, Q. Zhang, Y. Liu, J. Chen, H. Liu, Z. Guo, *Adv. Funct. Mater.* **2017**, 27, 1702634.
- [18] X. Ren, Q. Zhao, W. D. McCulloch, Y. Wu, *Nano Res.* **2017**, 10, 1313.

- [19] I. Sultana, M. M. Rahman, S. Mateti, V. G. Ahmadabadi, A. M. Glushenkov, Y. Chen, *Nanoscale* **2017**, 9, 3646.
- [20] Y. Dong, Z. Wu, S. Zheng, X. Wang, J. Qin, S. Wang, X. Shi, X. Bao, *ACS Nano* **2017**, 11, 4792.
- [21] P. Lian, Y. Dong, Z. Wu, S. Zheng, X. Wang, S. Wang, C. Sun, J. Qin, X. Shi, X. Bao, *Nano Energy* **2017**, 40, 1.
- [22] M. Naguib, R. A. Adams, Y. Zhao, D. Zemlyanov, A. Varma, J. Nanda, V. G. Pol, *Chem. Commun.* **2017**, 53, 6883.
- [23] a) Z. Jian, W. Luo, X. Ji, *J. Am. Chem. Soc.* **2015**, 137, 11566; b) M. S. Dresselhaus, G. Dresselhaus, *Adv. Phys.* **2006**, 30, 139; c) J. C. Chacón-Torres, L. Wirtz, T. Pichler, *Phys. Status Solidi B* **2014**, 251, 2337; d) J. R. Dahn, A. K. Sleight, H. Shi, J. N. Reimers, Q. Zhong, B. M. Way, *Electrochim. Acta* **1993**, 38, 1179.
- [24] J. Zhao, X. Zou, Y. Zhu, Y. Xu, C. Wang, *Adv. Funct. Mater.* **2016**, 26, 8103.
- [25] S. Komaba, T. Hasegawa, M. Dahbi, K. Kubota, *Electrochem. Commun.* **2015**, 60, 172.
- [26] W. Luo, J. Wan, B. Ozdemir, W. Bao, Y. Chen, J. Dai, H. Lin, Y. Xu, F. Gu, V. Barone, L. Hu, *Nano Lett.* **2015**, 15, 7671.
- [27] Z. Jian, Z. Xing, C. Bommier, Z. Li, X. Ji, *Adv. Energy Mater.* **2016**, 6, 1501874.
- [28] Z. Jian, S. Hwang, Z. Li, A. S. Hernandez, X. Wang, Z. Xing, D. Su, X. Ji, *Adv. Funct. Mater.* **2017**, 27, 1700324.
- [29] W. Wang, J. Zhou, Z. Wang, L. Zhao, P. Li, Y. Yang, C. Yang, H. Huang, S. Guo, *Adv. Energy Mater.* **2018**, 8, 1701648.
- [30] C. Chen, Z. Wang, B. Zhang, L. Miao, J. Cai, L. Peng, Y. Huang, J. Jiang, Y. Huang, L. Zhang, J. Xie, *Energy Storage Mater.* **2017**, 8, 161.
- [31] Y. Xie, Y. Chen, L. Liu, P. Tao, M. Fan, N. Xu, X. Shen, C. Yan, *Adv. Mater.* **2017**, 29, 1702268.

- [32] X. Zhao, P. Xiong, J. Meng, Y. Liang, J. Wang, Y. Xu, *J. Mater. Chem. A* **2017**, 5, 19237.
- [33] J. Yang, Z. Ju, Y. Jiang, Z. Xing, B. Xi, J. Feng, S. Xiong, *Adv. Mater.* **2018**, 30, 1700104.
- [34] M. Chen, W. Wang, X. Liang, S. Gong, J. Liu, Q. Wang, S. Guo, H. Yang, *Adv. Energy Mater.* **2018**, 1800171.
- [35] K. Share, A. P. Cohn, R. Carter, B. Rogers, C. L. Pint, *ACS Nano* **2016**, 10, 9738.
- [36] Z. Tai, Q. Zhang, Y. Liu, H. Liu, S. Dou, *Carbon* **2017**, 123, 54.
- [37] Z. Xing, Y. Qi, Z. Jian, X. Ji, *ACS Appl. Mater. Inter.* **2017**, 9, 4343.
- [38] X. Bie, K. Kubota, T. Hosaka, K. Chihara, S. Komaba, *J. Mater. Chem. A* **2017**, 5, 4325.
- [39] A. Eftekhari, *Energy Storage Mater.* **2017**, 7, 157.
- [40] H. Wang, T. Abe, S. Maruyama, Y. Iriyama, Z. Ogumi, K. Yoshikawa, *Adv. Mater.* **2005**, 17, 2857.
- [41] X. Wang, X. Xu, C. Niu, J. Meng, M. Huang, X. Liu, Z. Liu, L. Mai, *Nano Lett.* **2016**, 17, 544.
- [42] S. Zhang, J. Niu, H. Song, L. Zhu, J. Zhou, X. Chen, J. Liu, S. Hong, R. Song, *J. Mater. Chem. A* **2013**, 1, 14103.
- [43] K. Tang, L. Fu, R. J. White, L. Yu, M. Titirici, M. Antonietti, J. Maier, *Adv. Energy Mater.* **2012**, 2, 873.
- [44] Y. Cao, L. Xiao, M. L. Sushko, W. Wang, B. Schwenzer, J. Xiao, Z. Nie, L. V. Saraf, Z. Yang, J. Liu, *Nano Lett.* **2012**, 12, 3783.
- [45] Z. Wang, L. Zhou, X. W. Lou, *Adv. Mater.* **2012**, 24, 1903.
- [46] X. W. Lou, C. M. Li, L. A. Archer, *Adv. Mater.* **2009**, 21, 2536.
- [47] Y. Mao, H. Duan, B. Xu, L. Zhang, Y. Hu, C. Zhao, Z. Wang, L. Chen, Y. Yang, *Energy Environ. Sci.* **2012**, 5, 7950.

- [48] H. Liu, M. Jia, S. Yue, B. Cao, Q. Zhu, N. Sun, B. Xu, *J. Mater. Chem. A* **2017**, 5, 9572.
- [49] B. Cao, H. Liu, B. Xu, Y. Lei, X. Chen, H. Song, *J. Mater. Chem. A* **2016**, 4, 6472.
- [50] Y. Chen, L. Shi, A. Li, S. Zhang, M. Guo, X. Chen, J. Zhou, H. Song, *J. Electrochem. Soc.* **2017**, 164, A2000.
- [51] Y. Chen, L. Shi, S. Guo, Q. Yuan, X. Chen, J. Zhou, H. Song, *J. Mater. Chem. A* **2017**, 5, 19866.
- [52] P. Simon, Y. Gogotsi, B. Dunn, *Science* **2014**, 343, 1210.
- [53] J. Wang, J. Polleux, J. Lim, B. Dunn, *J. Phys. Chem. C* **2007**, 111, 14925.
- [54] D. Pech, M. Brunet, H. Durou, P. Huang, V. Mochalin, Y. Gogotsi, P. Taberna, P. Simon, *Nat. Nanotechnol.* **2010**, 5, 651.

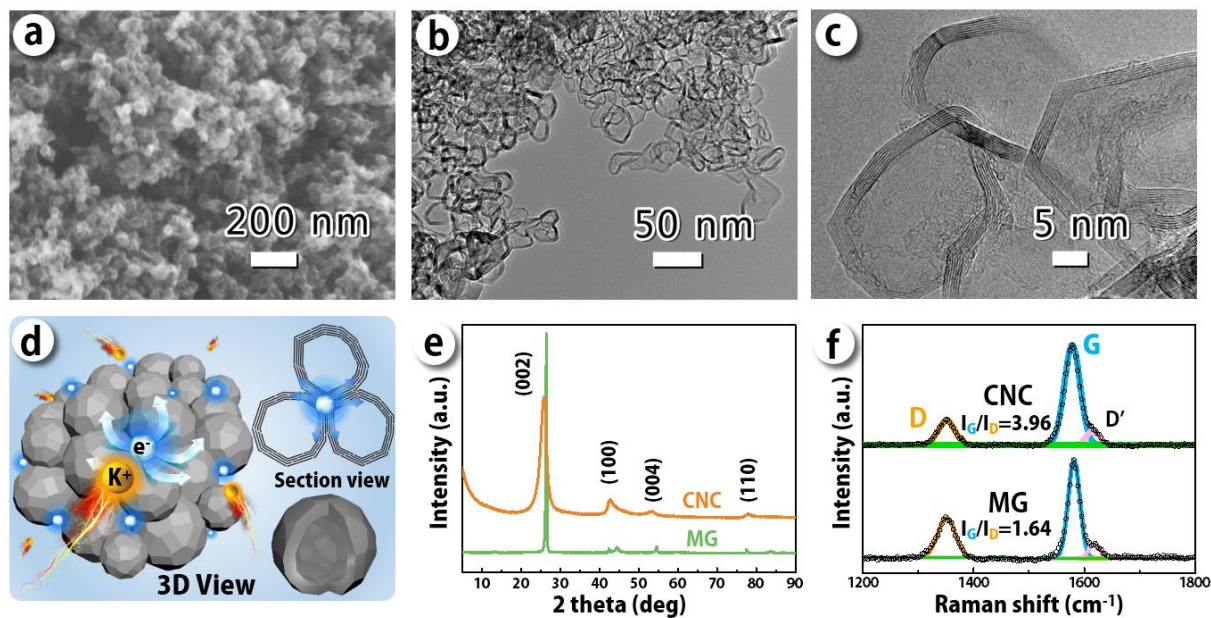


Figure 1. SEM image (a), HRTEM images (b and c), and schematic illustration of the structure (d) of CNC. XRD patterns (e) and Raman spectra (f) of CNC and MG.

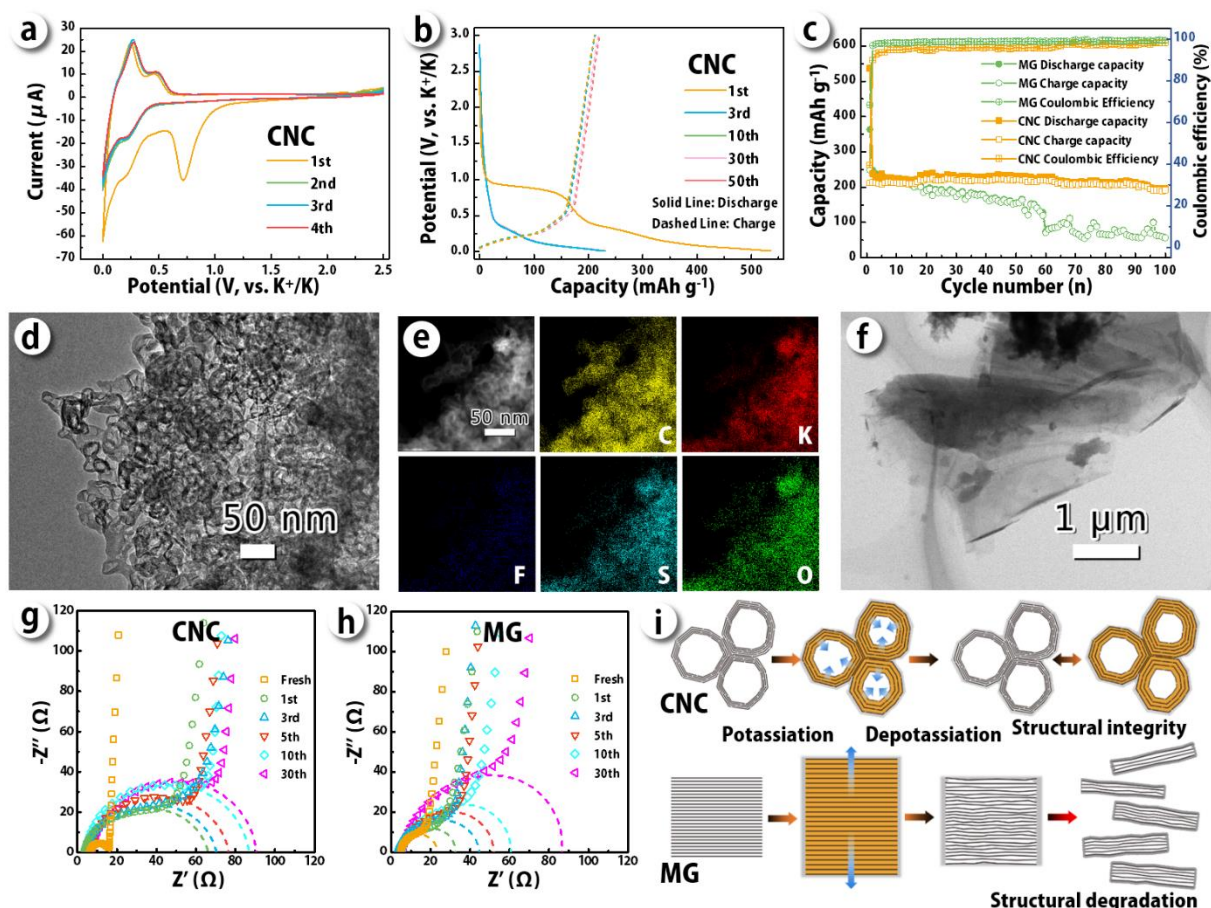


Figure 2. Electrochemical properties. CV curves at the scan rate of 0.1 mV s^{-1} (a) and voltage profiles (b) at 0.2 C ($1 \text{ C} = 279 \text{ mA g}^{-1}$) of CNC. (c) Galvanostatic cycling at 0.2 C of CNC and MG. HRTEM image (d) and high-angle annular dark-field image with corresponding EDS maps (e) of CNC. HRTEM image of MG (f) after 100 cycles at 0.2 C. Electrochemical impedance spectra (Nyquist plots) of CNC (g) and MG (h) electrodes after different cycles in symmetric cells. Schematic illustration of structural variations of CNC and MG electrodes during potassium storage (i).

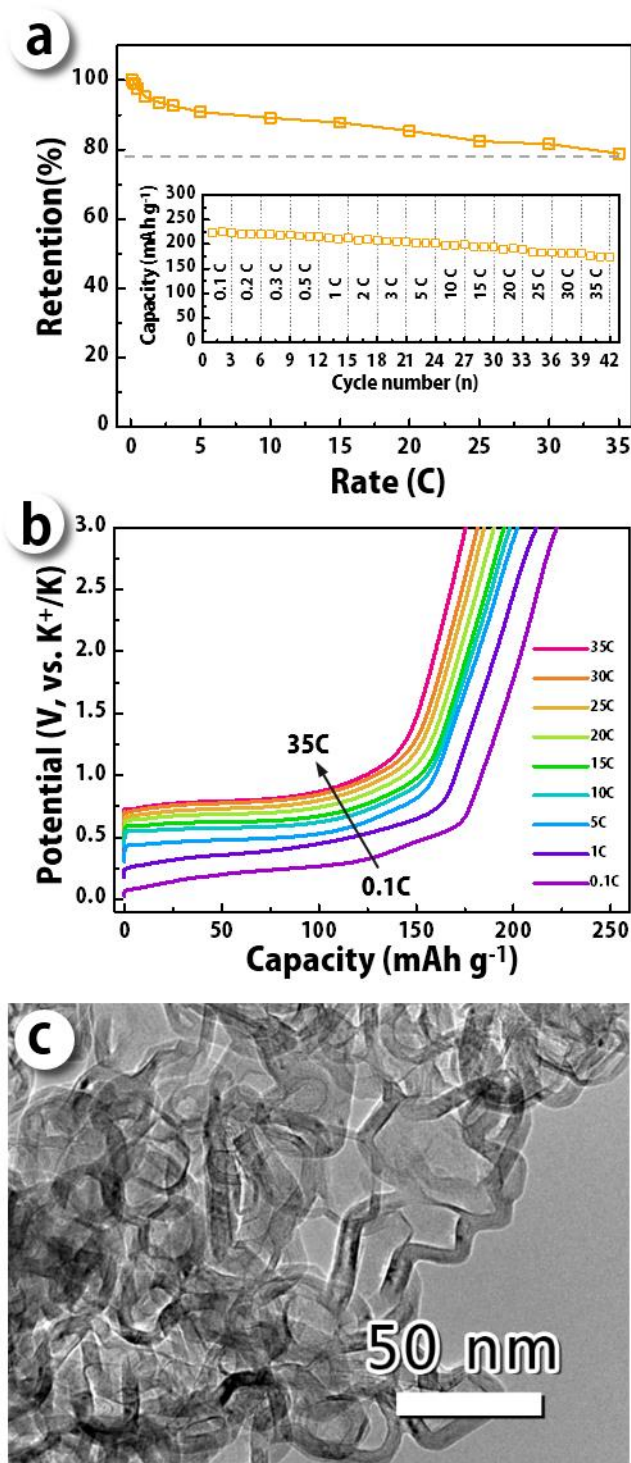


Figure 3. Retention of depotassiation capability with rate capability shown in the inset (a), and voltage profiles at different depotassiation rates (b) of CNC electrode. HRTEM image of CNC electrode after depotassiation at the high rate of 35 C (c).

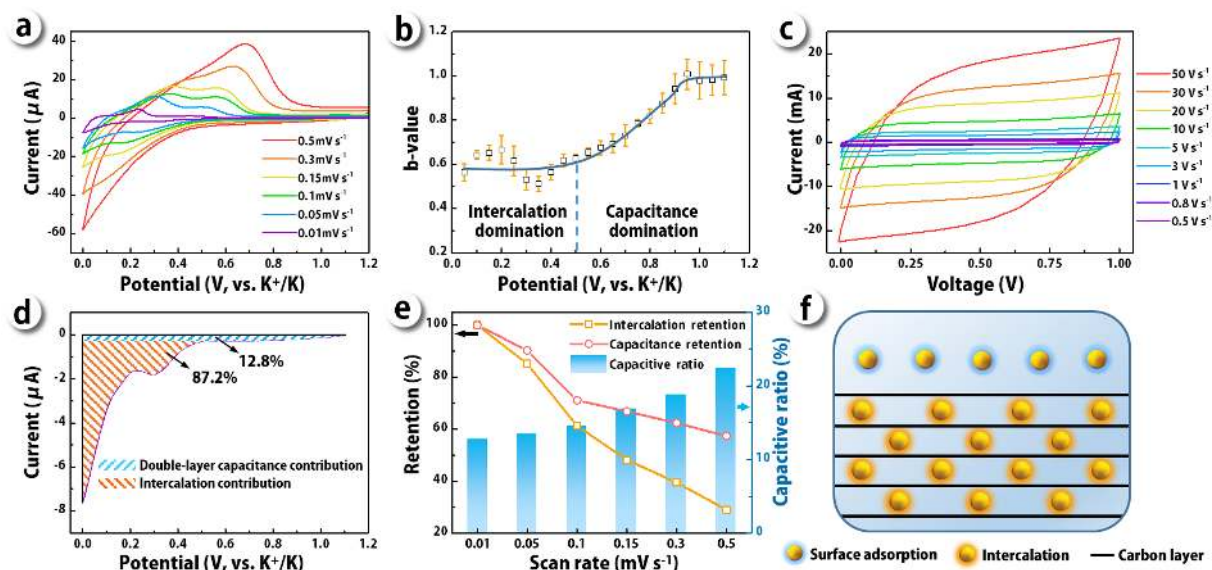


Figure 4. Electrochemical kinetic analysis of potassium storage behavior of CNC electrodes. (a) CV curves at different scan rates. (b) b-values plotted as a function of potential for the cathodic scan (K^+ intercalation). (c) CV curves of CNC symmetric cell at high scan rates. (d) Separation of the double-layer capacitance contribution in the cathodic scan of CNC with potential window of 0-1.1 V at a scan rate of 0.01 mV s^{-1} . (e) Double-layer capacitance contribution and its capacity retention at different scan rates. (f) Schematic illustration of the hybrid potassium storage behavior in CNC electrode.

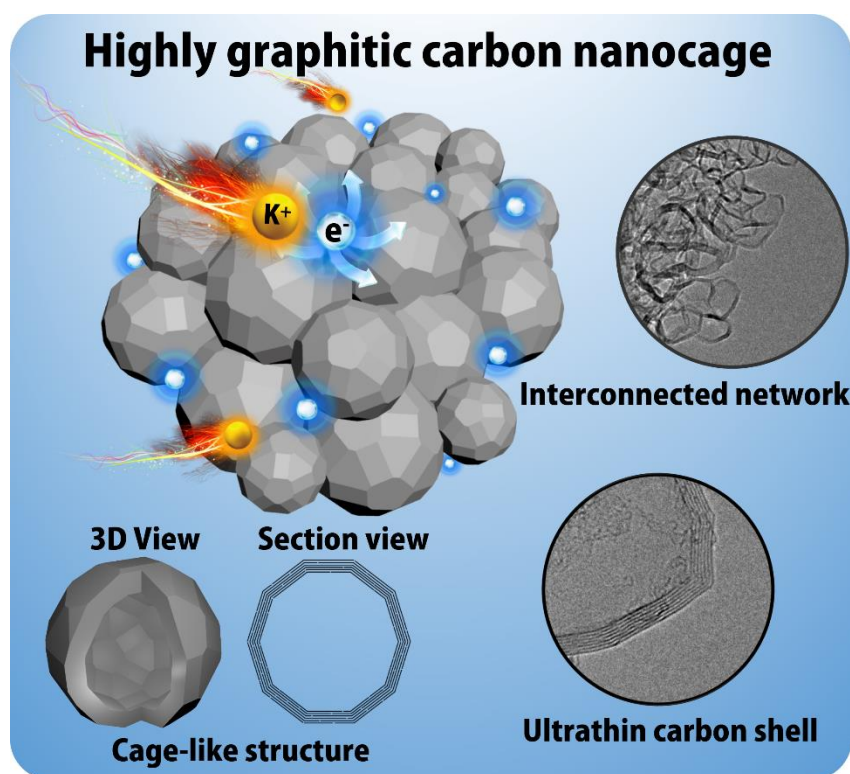
The table of contents entry

Highly graphitic carbon nanocage is reported as an anode material of potassium-ion batteries and exhibits excellent cyclability and superior depotassiation capacity of 175 mAh g^{-1} at $35 \text{ }^{\circ}\text{C}$. The potassium storage mechanism in carbon nanocage was revealed by cyclic voltammetry as due to redox reactions (intercalation/de-intercalation) and double-layer capacitance (surface adsorption/desorption).

Keyword: Potassium-ion batteries, anode, carbon nanocage, cyclability, rate capability

Bin Cao, Qing Zhang, Huan Liu, Bin Xu,* Shilin Zhang, Tengfei Zhou, Jianfeng Mao, Wei Kong Pang, Zaiping Guo,* Ang Li, Jisheng Zhou, Xiaohong Chen, Huaihe Song*

Title: Graphitic carbon nanocage as a stable and high power anode for potassium-ion batteries



TOC Figure

Supporting Information

Graphitic carbon nanocage as a stable and high power anode for potassium-ion batteries

Bin Cao, Qing Zhang, Huan Liu, Bin Xu, Shilin Zhang, Tengfei Zhou, Jianfeng Mao, Wei Kong Pang, Zaiping Guo,* Ang Li, Jisheng Zhou, Xiaohong Chen, Huaihe Song**

Bin Cao, Dr. Ang Li, Prof. Jisheng Zhou, Prof. Xiaohong Chen, Prof. Huaihe Song
State Key Laboratory of Chemical Resource Engineering, Beijing Key Laboratory of
Electrochemical Process and Technology for Materials, Beijing University of Chemical
Technology, Beijing 100029, China
E-mail: songhh@mail.buct.edu.cn

Dr. Huan Liu, Prof. Bin Xu
State Key Laboratory of Organic-Inorganic Composites, Beijing Key Laboratory of
Electrochemical Process and Technology for Materials, Beijing University of Chemical
Technology, Beijing 100029, China
E-mail: binxumail@163.com

Bin Cao, Qing Zhang, Shilin Zhang, Dr. Tengfei Zhou, Dr. Jianfeng Mao, Dr. Wei Kong
Pang, Prof. Zaiping Guo
Institute for Superconducting and Electronic Materials, School of Mechanical, Materials and
Mechatronics Engineering, University of Wollongong, North Wollongong, NSW 2500,
Australia
E-mail: zguo@uow.edu.au

Experimental Section

Materials Synthesis. CNC was synthesized by high temperature treatment of Ketjen carbon black (EC300J) at 2800°C under Ar atmosphere. Mesophase graphite (MG) with an average particle size of 8.4 μm was prepared in our laboratory by polycondensation from coal tar pitch and graphitization at 2800°C.

Materials characterization. The morphologies of CNC and MG were observed by field-emission scanning electron microscopy (FESEM, ZEISS SUPRATM 55) and high-resolution transmission electron microscopy (HRTEM, JEM-2010 and ARM-200F, JEOL). Raman spectroscopy (Renishaw inVia Reflex using 514 nm laser excitation) and X-ray diffraction (XRD, Rigaku D/max-2500B2+/PC system with Cu K α radiation) were used to characterize the crystal structures. Nitrogen adsorption–desorption measurements were performed at 77 K on a Micromeritics ASAP2046 to evaluate the Brunauer-Emmett-Teller (BET) specific surface area and pore volume. The samples were degassed at 300°C for 10 h under vacuum before sorption measurements.

Electrochemical measurements. Coin-type cell (CR2032) were assembled in an argon-filled glove box with electrodes and a glass fiber separator. The working electrodes were prepared by coating the slurry onto copper foil and then drying it under vacuum at 120°C for 12 h. The slurry of CNC was prepared by mixing 91 wt.% active materials with 9 wt.% binder (3 wt.% sodium carboxymethyl cellulose (CMC) and 6 wt.% poly(acrylic acid) (PAA)) in deionized water. The MG slurry was prepared by mixing 81 wt.% active materials, 10 wt.% conducting agent (Super P), and 9 wt.% binder (3 wt.% CMC and 6 wt.% PAA) in deionized water. The active material loading was $\sim 0.8\text{--}1\text{ mg cm}^{-2}$. The electrolyte solutions used in this study were 1 M KN(SO₂F)₂ (KFSI) in ethylene carbonate: propylene carbonate (EC: PC, 1:1 by volume) and 1 M LiPF₆ in EC: dimethyl carbonate: ethyl methyl carbonate (EC: DMC: EMC, 1:1:1 by volume). The half-cells were fabricated in the following order: the carbon electrode, the glass fiber separator, and a piece of alkali metal foil (K or Li) as the counter and reference electrode with the corresponding electrolyte. Symmetric cells were prepared with same electrodes on the anode and cathode side, such as potassium/potassium or CNC/CNC, glass fiber separator and corresponding electrolyte. The galvanostatic discharge/charge cycling and depotassiation capability of CNC were measured between 0.01 and 3.0 V vs. K⁺/K by using Neware and Arbin battery testers. Cyclic voltammetry (CV) and electrochemical impedance spectroscopy (EIS) were carried out on a VMP-3 electrochemical workstation. EIS was carried out with an amplitude of 5.0 mV in the frequency range of 200 kHz to 10 mHz with the open circuit potential depending on the type of cell (above 2 V for uncycled half-cells, 0 V for symmetric

cells). The galvanostatic intermittent titration technique (GITT) testing was performed using current pulses with a duration (0.1 C) of 0.5 h and a relaxation process over 5 h.

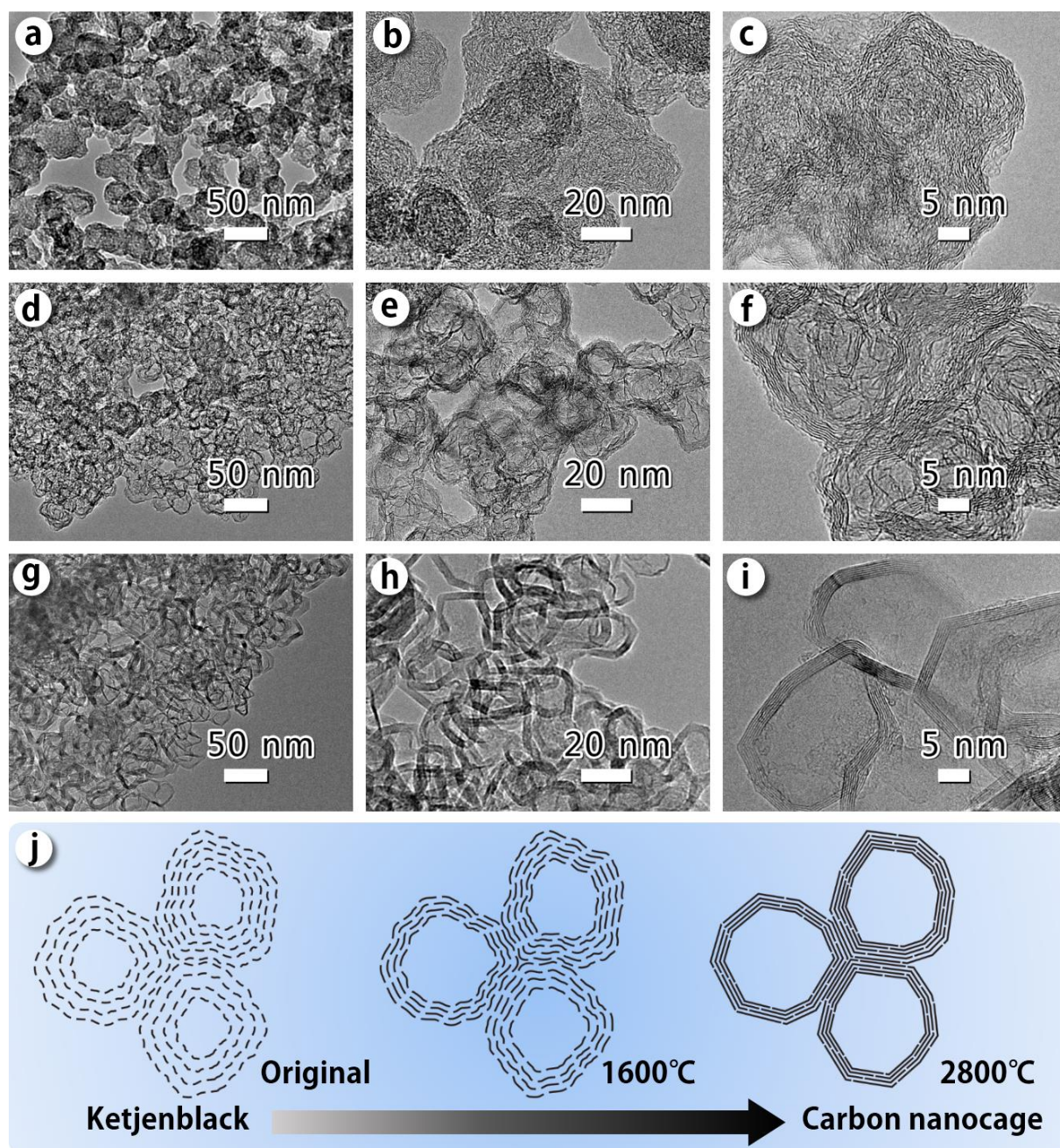


Figure S1. HRTEM images of original Ketjen carbon black (a-c), Ketjen carbon black-1600 (heat treated at 1600°C) (d-f) and CNC (g-i). Schematic illustration of the structural transformation from Ketjenblack to CNC during heat-treatment (j).

As seen in HRTEM images in [Figure S1](#) a-c, although Ketjen carbon black has an amorphous structure, its small basic structural carbon units (BSCU) are arranged concentrically and thus

exhibit the characteristic of short range order. After heat-treatment at 1600 °C, the BSCU in Ketjen carbon black-1600 (**Figure S1d-f**) has a relatively larger crystal size than that in the original Ketjen carbon black, which is ascribed to the growth of and connections among different BSCU. Meanwhile, the hollow structure of Ketjen carbon black-1600 can be clearly observed. Finally, after heat-treatment in 2800°C, the CNC with a developed layered structure and hollow cage-like structure is formed. The different CNCs are interconnected into a complex net structure. The structural transformation from Ketjen carbon black to highly graphitic CNC is briefly illustrated in **Figure S1j**.

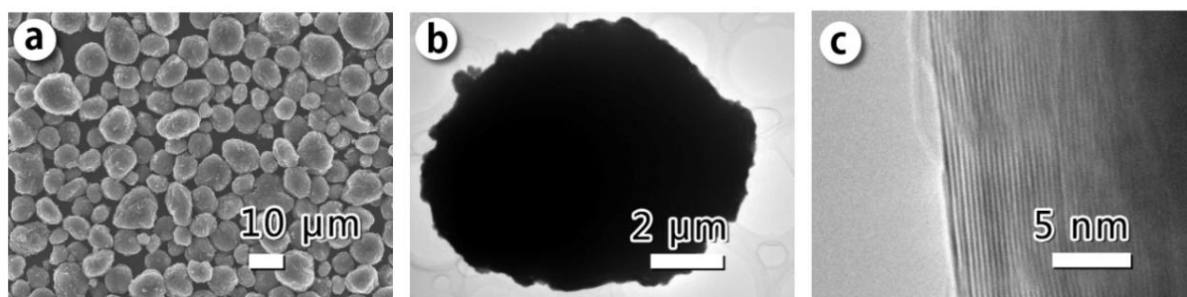


Figure S2. SEM image (a) and HRTEM images (b and c) of MG.

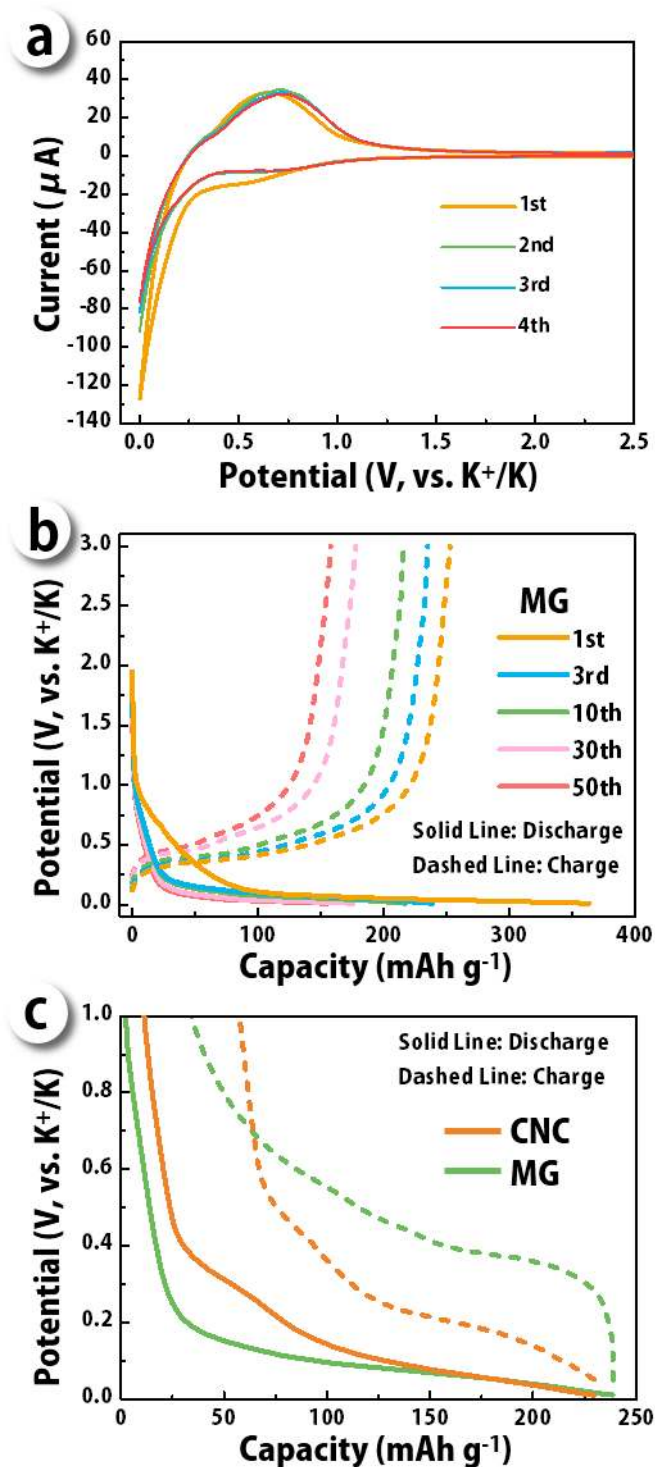


Figure S3. CV curves for the initial 4 cycles at the scan rate of 0.1 mV s^{-1} (a) and voltage profiles for selected cycles (b) at 0.2 C ($1 \text{ C} = 279 \text{ mA g}^{-1}$) of MG. Voltage profiles (c) of CNC and MG show the voltage hysteresis between the charge and discharge curves at 0.2 C .

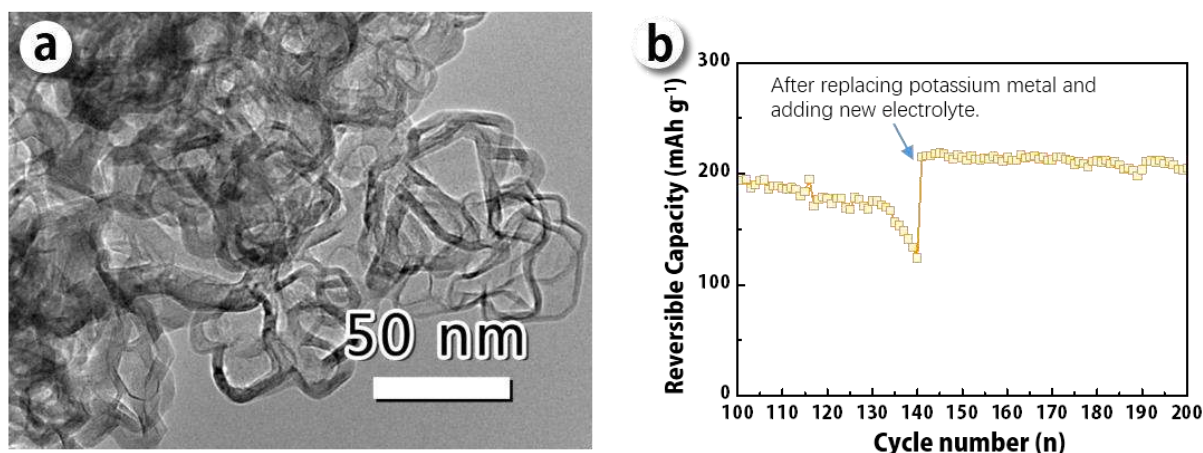


Figure S4. HRTEM image of CNC electrode after 140 cycles at 0.2 C (a) and the cyclability after 100 cycles (b).

CNC electrode in potassium half-cell exhibits obvious capacity fading after ~140 cycles, and then the electrode was characterized by HRTEM (shown in [Figure S4a](#)). It can be seen that the structure of CNC after 140 cycles remains the same as that of the CNC electrodes after 100 cycles ([Figure 2d](#)). Moreover, structural degradation or exfoliation were not found. If we replace the potassium metal and add new electrolyte to the cell after 140 cycles, the cell can cycle again ([Figure S4b](#)). Therefore, the capacity fading after 140 cycles can be ascribed to the degradation of the potassium metal electrode or the drying out of electrolyte. Potassium has high chemical activity and can react with the organic electrolyte to generate a thick solid-electrolyte interphase layer (the thick purple layer shown in [Figure S8d](#)), thus consuming the limited amount of electrolyte. Long-term cycling is another challenge in PIBs in half-cell configurations. Since CNC could maintain its structural integrity over 100 cycles, CNC should have a good long term cycling performance due its high structural stability.

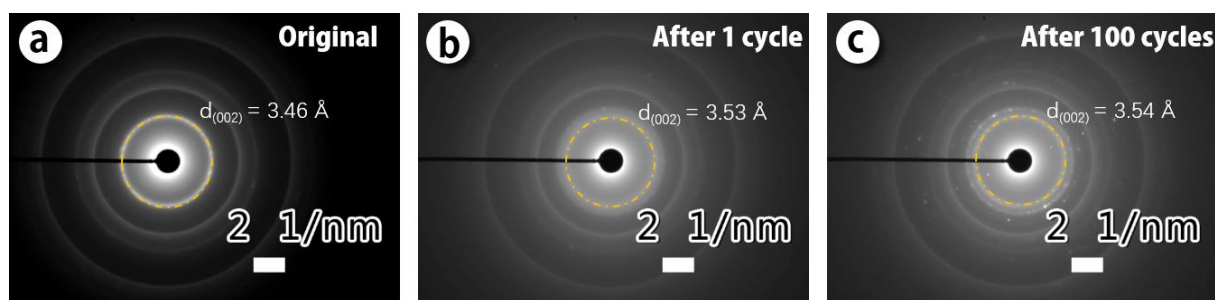


Figure S5. SAED patterns of initial CNC (a) and CNC after 1 cycle (b) and 100 cycles (c).

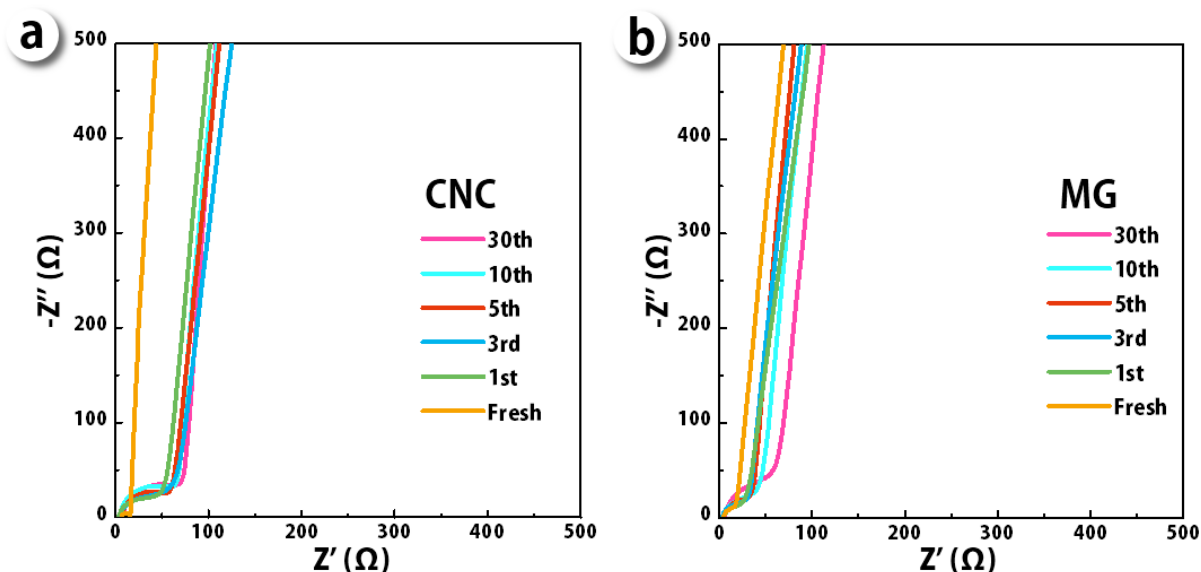


Figure S6. Nyquist plots of CNC and MG electrodes after selected cycles in symmetric cells.

Potassium half-cells usually have high impedance properties,^[1] which should be ascribed to the high activity of potassium metal.^[2,3] Potassium metal can react with organic electrolyte and generate a thick solid-electrolyte interphase layer, as shown in [Figure S8](#). The impedance properties of the working electrode in a potassium half-cell would be masked by the large impedance of potassium metal electrode. Therefore, symmetric cells would be a good choice for EIS testing, as it can avoid the interference from the large impedance of potassium metal electrode. After different cycles, the electrodes were charged to 3 V in a potassium half-cell to ensure the full depotassiation state, and then the half-cells were disassembled for assembly in symmetric cells. As shown in [Figure S6](#), the Nyquist plots typically consist of semicircles and a nearly vertical line with respect to the Z' -axis. The semicircle mainly reflects the interfacial impedance features of fresh electrodes and cycled electrodes. The nearly vertical line corresponds to the capacitive reactance,^[4] as typical electrical blocking behavior, rather than the ion diffusion because the carbon matrix is highly de-intercalated.

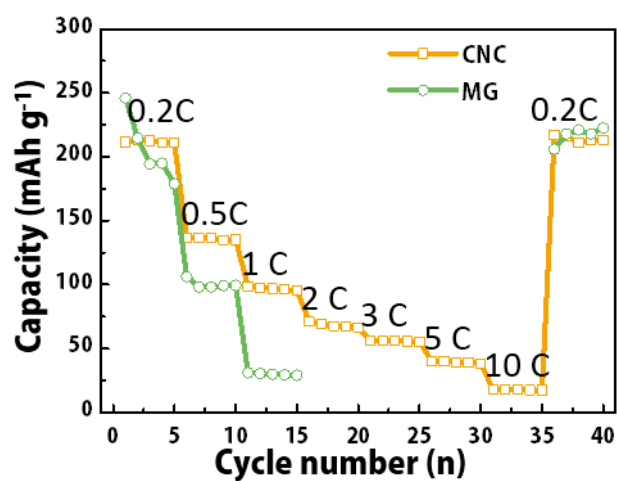


Figure S7. Rate performance of CNC and MG with charge/discharge at the same rates.

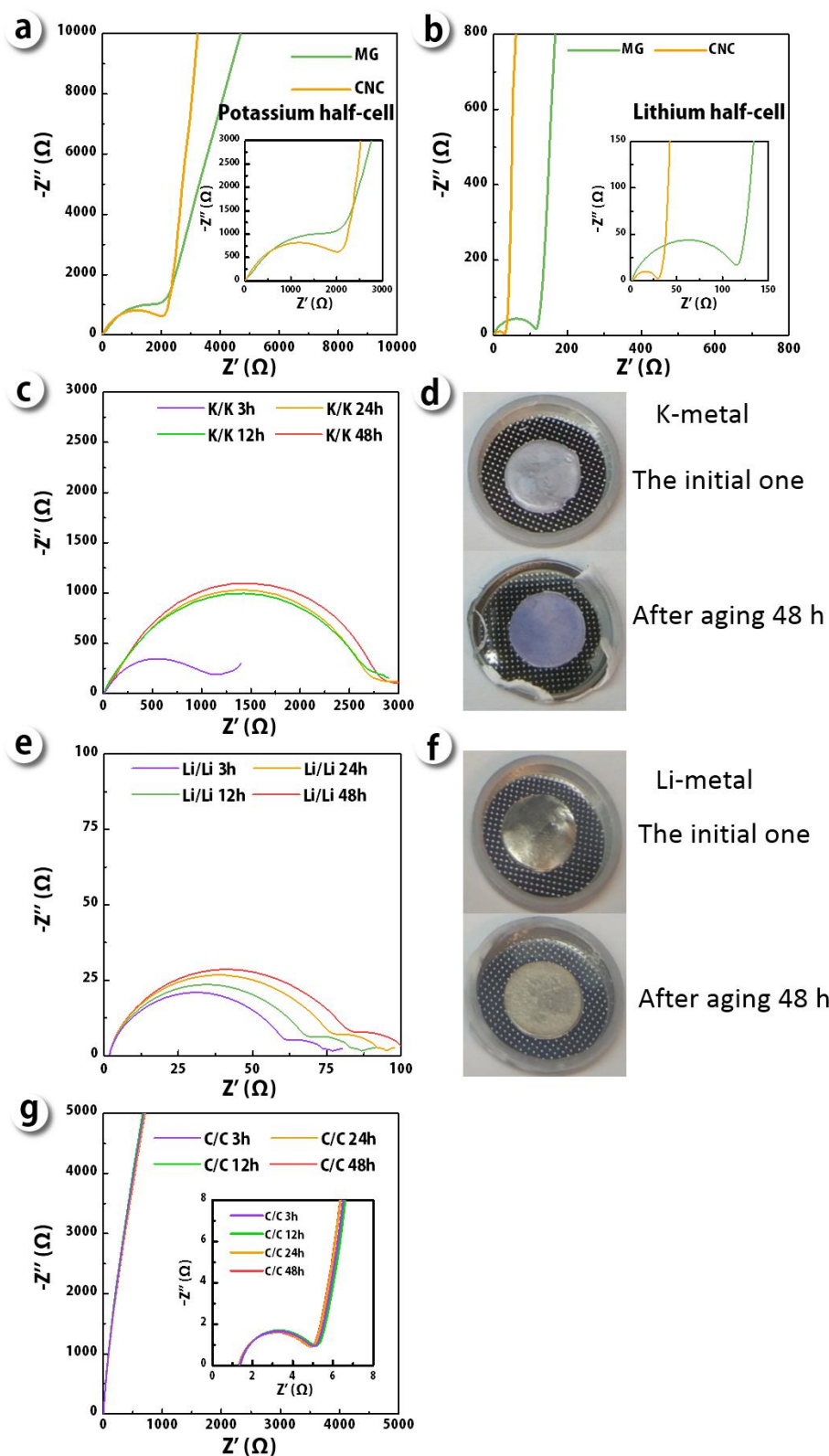


Figure S8. Electrochemical impedance properties. Nyquist plots of CNC and MG electrodes in potassium half-cell (a) and lithium half-cell (b) after aging for 24 h. (c) Nyquist plots of potassium metal symmetric cell (K/K) after different aging times. (d) Digital images of potassium metal electrode in the initial state and after aging 48 h. (e) Nyquist plots of lithium metal symmetric cell (Li/Li) after different aging times. (f) Digital images of lithium metal electrode in the initial state and after aging for 48 h. (g) Nyquist plots of CNC symmetric cell (C/C) after different aging times.

Figure S8a shows the Nyquist plots of the fresh electrodes of CNC and MG in potassium half-cells with aging for 24 h after assembly. Both CNC and MG show a semicircle with a large diameter, suggesting high impedance properties. However, the Nyquist plots of CNC and MG electrodes in lithium metal half-cells show a much smaller semicircle (**Figure S8b**). In order to reveal the large impedance in potassium metal half-cells, potassium metal (K/K), lithium metal (Li/Li) and CNC (C/C) symmetric cells were assembled and characterized by EIS.^[5] As shown in **Figure S8c**, e and g, symmetric cells show a semicircle that should be ascribed to the electrode/electrolyte interface.^[6] The diameter of the semicircle in the K/K cell increased quickly in the first 12 h and remained almost stable after 24 h. The high impedance of the interface between the potassium and the electrolyte was ascribed to the high activity of potassium metal because potassium metal can react with organic electrolyte and generate a thick solid-electrolyte interphase layer (shown in **Figure S8d** with a thick purple layer), thus resulting in large impedance.^[2,3] In comparison, the impedance arc of the C/C cell was almost unchanged after different aging times (**Figure S8g**), indicating carbon electrodes are stable in organic electrolyte. These results are consistent with earlier reports.^[1,7] Moreover, the Nyquist plots of the lithium metal symmetric cell (Li/Li cell) show a small semicircle, and its diameter did not increase significantly with aging time (**Figure S8e** and f). Therefore, the high impedance of the potassium half-cell should be ascribed to potassium metal due to its high chemical activity. Considering that the impedance in the potassium half-cell is the total impedance of the working electrode and the potassium metal electrode at the same frequencies,^[5,6] the impedance properties of the working electrode would be masked by the large impedance of the potassium metal electrode.

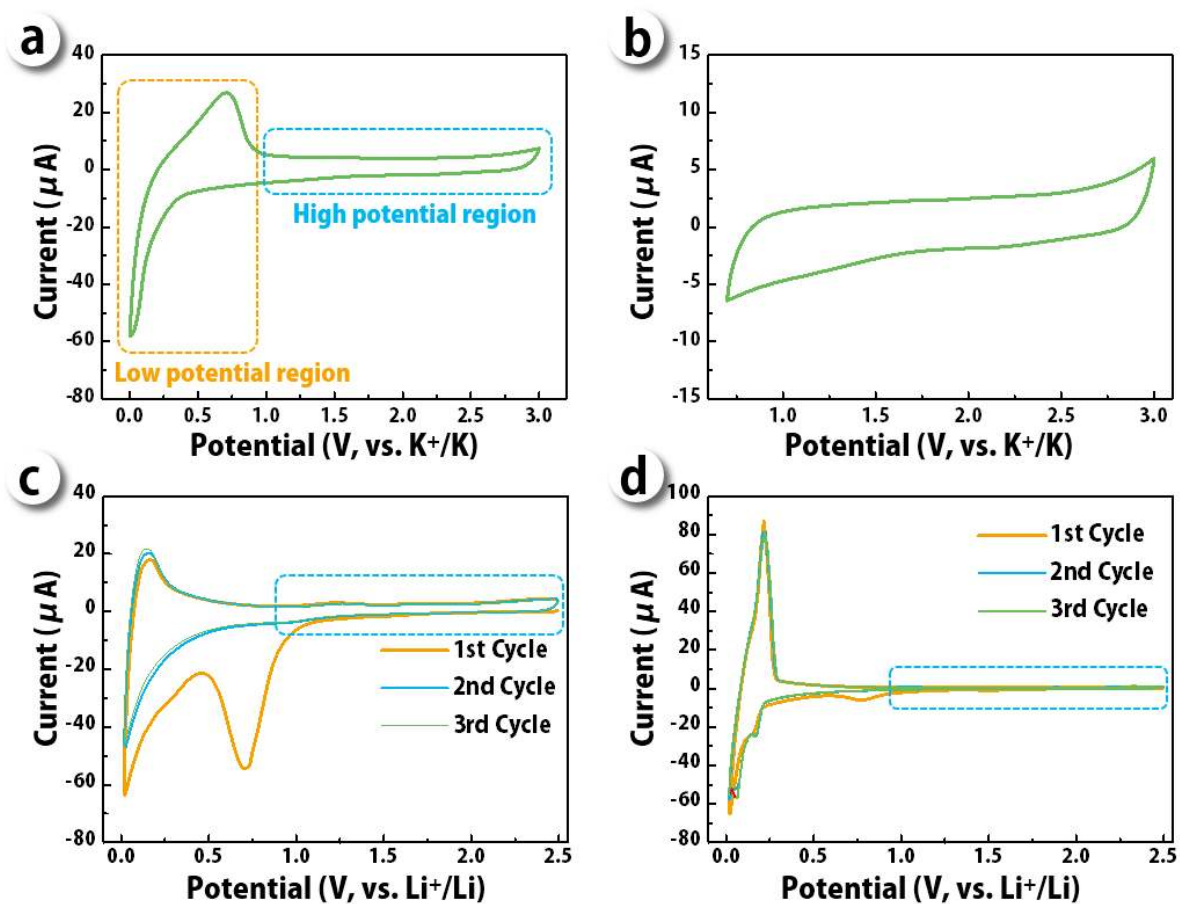


Figure S9. CV curves of CNC electrode in potassium half-cells with potential window of 0-3.0 V (a) and 0.7-3.0 V (b) at the scan rate of 0.3 mV s^{-1} . CV curves at scan rate of 0.1 mV s^{-1} for CNC electrode (c) and MG electrode (d) in lithium half-cells.

If the cell voltage is linearly proportional to $\sqrt{\tau}$ (**Figure S10**), the diffusion coefficient (D) in CNC electrodes can be calculated from the GITT potential profiles by Fick's second law with the following equation:

$$D = \frac{4}{\pi\tau} \left(\frac{m_B V_M}{M_B S} \right)^2 \left(\frac{\Delta E_S}{\Delta E_\tau} \right)^2, \quad (\text{Equation S1})$$

where τ is the duration of the current pulse; m_B is the electrode active material mass; S is the geometric area of the electrode; ΔE_S is the quasi-thermodynamic equilibrium potential difference before and after the current pulse; ΔE_τ is the potential difference during current pulse; V_M is the molar volume of the CNC; M_B is the molar mass of carbon. The value of M_B/V_M can be obtained from the density of CNC.

The density of CNC was calculated according to the following equation:

$$\rho = \frac{1}{V_{total} + \frac{1}{\rho_{Carbon}}}, \quad (\text{Equation S2})$$

where ρ (g cm^{-3}) is the density of CNC, V_{total} ($\text{cm}^3 \text{ g}^{-1}$) is the total pore volume measured from the N_2 isotherm, ρ_{Carbon} is the true density of carbon (2 g cm^{-3}). Since the V_{total} of CNC is $0.71 \text{ cm}^3 \text{ g}^{-1}$, the ρ of CNC is calculated to be 0.83 g cm^{-3} .

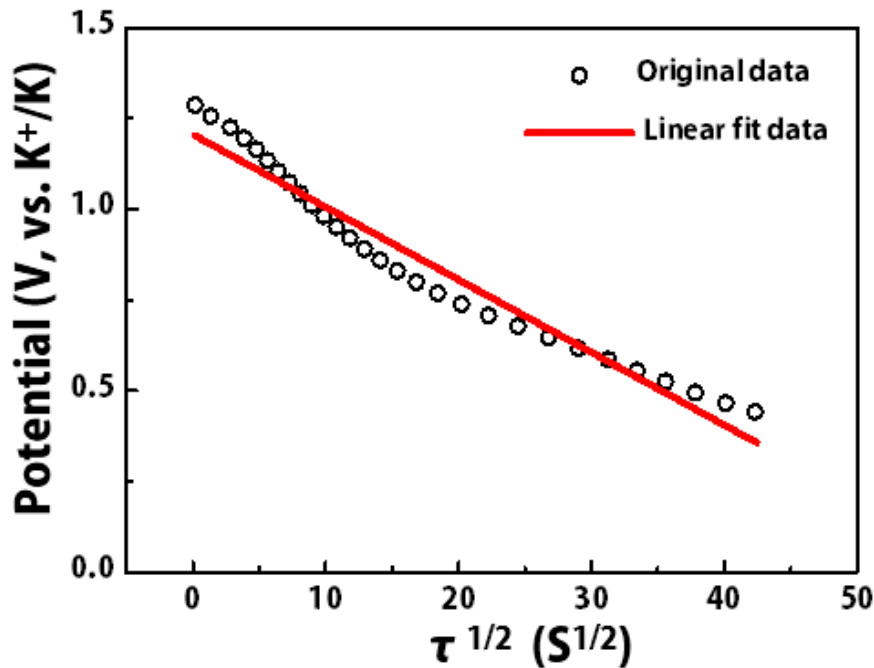


Figure S10. Linear behavior of the potential vs. $\tau^{1/2}$ in GITT at 1.287 V vs. K^+/K of CNC.

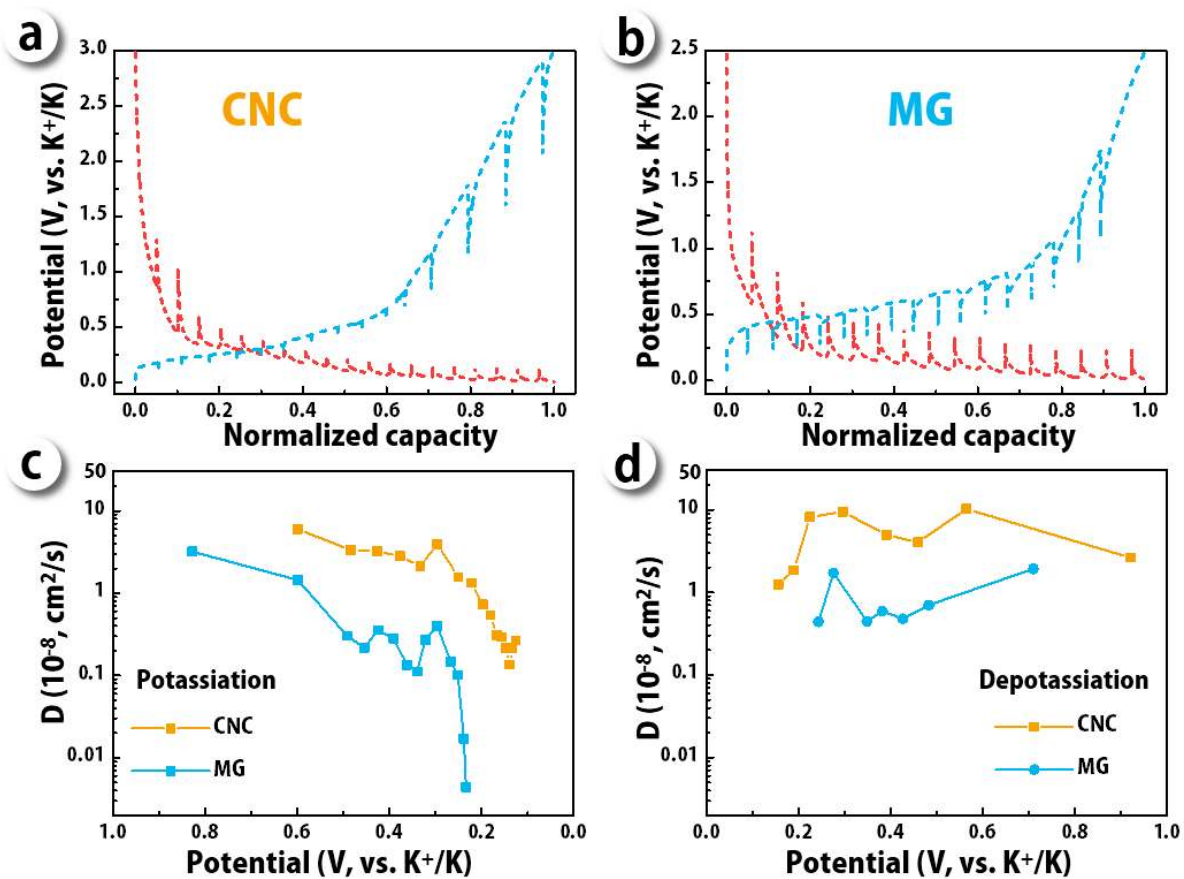


Figure S11. GITT potential profiles for CNC (a) and MG (b). Diffusion coefficients calculated from GITT potential profiles as a function of potential (c for potassiation and d for depotassiation).

Table S1 Summary of the electrochemical performance of CNC and reported state-of-art carbon anodes for PIBs.

Material	Main electrochemical behavior	Potassium storage potential	Cyclability	Rate performance	Reference
CNC	intercalation/de-intercalation	low	195 mAh g ⁻¹ with a high capacity retention of 92% after 100 cycles at 0.2 C 205 mAh g ⁻¹ with a high capacity retention of 97% after 200 cycles at 0.2 C (Replacing K metal and electrolyte after 140 cycles)	175 mAh g ⁻¹ at an ultrahigh rate of 35 C (potassiated at 0.1 C and depotassiated at 35 C) 40 mAh g ⁻¹ at 5 C (charge/discharge at the same current density)	This work
Synthetic graphite (TIMCAL TIMREX SLP50)	intercalation/de-intercalation	low	100 mAh g ⁻¹ with a capacity retention of 51% after 50 cycles at 0.5C	~10 mAh g ⁻¹ at 5 C	[8]
Natural graphite powder	intercalation/de-intercalation	low	~250 mAh g ⁻¹ with no capacity degradation after 50 cycles at 25 mA g ⁻¹	~240 mAh g ⁻¹ at an high rate of 15 C (potassiated at 0.1 C and depotassiated at 15 C)	[31]
KS4 conducting agent	intercalation/de-intercalation	low	220 mAh g ⁻¹ with a capacity retention of 89% after 200 cycles at 20 mA g ⁻¹	60 mAh g ⁻¹ at 200 mA g ⁻¹	[1]
Graphite	intercalation/de-intercalation	low	34 mAh g ⁻¹ with a capacity retention of 14% after 50 cycles at 1.5 mA g ⁻¹	-	[9]
Few layered graphene	intercalation/de-intercalation	low	140 mAhg ⁻¹ with a capacity retention of 67% after 100 cycles at 100 mA g ⁻¹	~ 5 mAh g ⁻¹ at 200 mA g ⁻¹	[10]
Nitrogen-doped graphene	intercalation/de-intercalation	low	210 mAhg ⁻¹ with a capacity retention of 78% after 100 cycles at 100 mA g ⁻¹	~ 50 mAh g ⁻¹ at 200 mA g ⁻¹	[11]
Polynanocrystalline Graphite	insertion/deinsert ion	medium	~ 60 mAh g ⁻¹ with a capacity retention of 50% after 300 cycles at 100 mA g ⁻¹	~ 50 mAh g ⁻¹ at 500 mA g ⁻¹	[12]
Carbon nanofiber paper	insertion/deinsert ion	medium	270 mAh g ⁻¹ with no capacity decay after 80 cycles at 20 mA g ⁻¹	~ 100 mAh g ⁻¹ at 7.7 A g ⁻¹	[13]
PTCDA derived soft carbon	insertion/deinsert ion	high	~ 154.66 mAh g ⁻¹ with a capacity retention of 81% after 50 cycles at 2C	140 mAh g ⁻¹ at 5 C	[8]
Carbon black	insertion/deinsert ion	high	~ 210 mAh g ⁻¹ with a capacity retention of 75% after 350 cycles at 400 mA g ⁻¹	~ 15 mAh g ⁻¹ at 1 A g ⁻¹	[14]
Nitrogen-rich hard carbon	insertion/deinsert ion	high	205 mAh g ⁻¹ with no capacity decay after 200 cycles at 0.12 C	156 mAh g ⁻¹ at 18 C	[15]
Hard-soft composite carbon	insertion/deinsert ion	high	200 mAh g ⁻¹ with a capacity retention of 93% after 200 cycles at 0.2C	81 mAh g ⁻¹ at 10 C	[16]
Waste-Tire Rubber derived hard carbon (TC1600)	insertion/deinsert ion	high	141 mAh g ⁻¹ with a capacity retention of 78 %after 200 cycles at 0.5C	72 mAh g ⁻¹ at 2 C	[17]
Ordered mesoporous carbon	insertion/deinsert ion	high	257.4 mAh g ⁻¹ with a capacity retention of ~83% after 100 cycles at 50 mA g ⁻¹	146.5 mAh g ⁻¹ at 1 A g ⁻¹	[18]
Hard Carbon Microspheres	insertion/deinsert ion	high	216 mAh g ⁻¹ with a capacity retention of 83% after 100 cycles at 0.1 C	136 mAh g ⁻¹ at 5C	[19]
Carbon nanofibers	insertion/deinsert ion	high	60 mAh g ⁻¹ with a capacity retention of ~20% after 20 cycles at 50 mA g ⁻¹	-	[20]
Phosphorus and oxygen dual-doped graphene	insertion/deinsert ion	high	474 mAh g ⁻¹ with a capacity retention of 84% after 50 cycles at 50 mA g ⁻¹	165 mAh g ⁻¹ at 2 A g ⁻¹	[21]
N- and O-Rich carbon nanofiber (CNF-O)	insertion/deinsert ion	high	160 mAh g ⁻¹ with a capacity retention of 80% after 300 cycles at 1 C	70 mAh g ⁻¹ at 10 C	[22]

Ultra-high pyridinic N-doped porous carbon monolith	insertion/deinsert ion	high	322 mAh g ⁻¹ with a capacity retention of 77% after 120 cycles at 150 mA g ⁻¹	199 mAh g ⁻¹ at 2 A g ⁻¹	[23]
Nitrogen- and phosphorous co-doped carbon microspheres (NPCM)	insertion/deinsert ion	high	270 mAh g ⁻¹ with a capacity retention of ~90% after 90 cycles at 100 mA g ⁻¹	189 mAh g ⁻¹ at 5 A g ⁻¹	[24]
Few-layer F-doped graphene foam	insertion/deinsert ion	high	165.9 mAh g ⁻¹ with a capacity retention of 52% after 200 cycles at 500 mA g ⁻¹	212.6 mAh g ⁻¹ at 500 mA g ⁻¹	[25]
Nitrogen-doped carbon nanofibers	insertion/deinsert ion	high	215.2 mAh g ⁻¹ with a capacity retention of ~92% after 200 cycles at 0.2 C	84.7 mAh g ⁻¹ at 5 C	[26]
Sulfur/Oxygen Codoped Porous Hard Carbon Microspheres	insertion/deinsert ion	high	226.6 mAh g ⁻¹ with a capacity retention of ~98% after 100 cycles at 0.18 C	158 mAh g ⁻¹ at 1 A g ⁻¹	[27]
Nitrogen-Doped Carbon Nanotubes	insertion/deinsert ion	medium	254.7 mAh g ⁻¹ with a capacity retention of 86% after 300 cycles at 50 mA g ⁻¹	102 mAh g ⁻¹ at 2 A g ⁻¹	[28]
Nitrogen/Oxygen Dual-Doped Hard Carbon	insertion/deinsert ion	high	230.6 mAh g ⁻¹ with a capacity retention of 76% after 100 cycles at 50 mA g ⁻¹	118 mAh g ⁻¹ at 3 A g ⁻¹	[29]
N-doped hierarchically porous carbon	insertion/deinsert ion	high	296.8 mAh g ⁻¹ with a capacity retention of ~82% after 100 cycles at 50 mA g ⁻¹	193.1 mAh g ⁻¹ at 500 mA g ⁻¹	[30]

‘-’ stands for unknown value.

1 C = 279 mA g⁻¹.

Supporting References

- [1] J. Zhao, X. Zou, Y. Zhu, Y. Xu, C. Wang, *Adv. Funct. Mater.* **2016**, 26, 8103.
- [2] A. Eftekhari, Z. Jian, X. Ji, *ACS Appl. Mater. Inter.* **2017**, 9, 4404.
- [3] X. Wu, D. P. Leonard, X. Ji, *Chem. Mater.* **2017**, 29, 5031.
- [4] F. La Mantia, J. Vetter, P. Novák, *Electrochim. Acta* **2008**, 53, 4109.
- [5] R. Petibon, C. P. Aiken, N. N. Sinha, J. C. Burns, H. Ye, C. M. VanElzen, G. Jain, S. Trussler, J. R. Dahn, *J. Electrochem. Soc.* **2012**, 160, A117.
- [6] J. Y. Song, H. H. Lee, Y. Y. Wang, C. C. Wan, *J. Power Sources* **2002**, 111, 255.
- [7] W. D. McCulloch, X. Ren, M. Yu, Z. Huang, Y. Wu, *ACS Appl. Mater. Inter.* **2015**, 7, 26158.
- [8] Z. Jian, W. Luo, X. Ji, *J. Am. Chem. Soc.* **2015**, 137, 11566.
- [9] J. C. Pramudita, V. K. Peterson, J. A. Kimpton, N. Sharma, *Powder Diffr.* **2017**, 32, S43.
- [10] K. Share, A. P. Cohn, R. E. Carter, C. L. Pint, *Nanoscale* **2016**, 8, 16435.

- [11] K. Share, A. P. Cohn, R. Carter, B. Rogers, C. L. Pint, *ACS Nano* **2016**, 10, 9738.
- [12] Z. Xing, Y. Qi, Z. Jian, X. Ji, *ACS Appl. Mater. Inter.* **2017**, 9, 4343.
- [13] X. Zhao, P. Xiong, J. Meng, Y. Liang, J. Wang, Y. Xu, *J. Mater. Chem. A* **2017**, 5, 19237.
- [14] Z. Tai, Y. Liu, Q. Zhang, T. Zhou, Z. Guo, H. K. Liu, S. X. Dou, *Green Energy Environ.* **2017**, 2, 278.
- [15] C. Chen, Z. Wang, B. Zhang, L. Miao, J. Cai, L. Peng, Y. Huang, J. Jiang, Y. Huang, L. Zhang, J. Xie, *Energy Storage Mater.* **2017**, 8, 161.
- [16] Z. Jian, S. Hwang, Z. Li, A. S. Hernandez, X. Wang, Z. Xing, D. Su, X. Ji, *Adv. Funct. Mater.* **2017**, 27, 1700324.
- [17] Y. Li, R. A. Adams, A. Arora, V. G. Pol, A. M. Levine, R. J. Lee, K. Akato, A. K. Naskar, M. P. Paranthaman, *J. Electrochem. Soc.* **2017**, 164, A1234.
- [18] W. Wang, J. Zhou, Z. Wang, L. Zhao, P. Li, Y. Yang, C. Yang, H. Huang, S. Guo, *Adv. Energy Mater.* **2018**, 8, 1701648.
- [19] Z. Jian, Z. Xing, C. Bommier, Z. Li, X. Ji, *Adv. Energy Mater.* **2016**, 6, 1501874.
- [20] Y. Liu, F. Fan, J. Wang, Y. Liu, H. Chen, K. L. Jungjohann, Y. Xu, Y. Zhu, D. Bigio, T. Zhu, C. Wang, *Nano Lett.* **2014**, 14, 3445.
- [21] G. Ma, K. Huang, J. Ma, Z. Ju, Z. Xing, Q. Zhuang, *J. Mater. Chem. A* **2017**, 5, 7854.
- [22] R. A. Adams, J. Syu, Y. Zhao, C. Lo, A. Varma, V. G. Pol, *ACS Appl. Mater. Inter.* **2017**, 9, 17872.
- [23] Y. Xie, Y. Chen, L. Liu, P. Tao, M. Fan, N. Xu, X. Shen, C. Yan, *Adv. Mater.* **2017**, 29, 1702268.
- [24] Y. Li, Z. Wang, L. Li, S. Peng, L. Zhang, M. Srinivasan, S. Ramakrishna, *Carbon* **2016**, 99, 556.
- [25] Z. Ju, S. Zhang, Z. Xing, Q. Zhuang, Y. Qiang, Y. Qian, *ACS Appl. Mater. Inter.* **2016**, 8, 20682.

- [26] R. Hao, H. Lan, C. Kuang, H. Wang, L. Guo, *Carbon* **2018**, 128, 224.
- [27] M. Chen, W. Wang, X. Liang, S. Gong, J. Liu, Q. Wang, S. Guo, H. Yang, *Adv. Energy Mater.* **2018**, 1800171.
- [28] P. Xiong, X. Zhao, Y. Xu, *ChemSusChem* **2018**, 11, 202.
- [29] J. Yang, Z. Ju, Y. Jiang, Z. Xing, B. Xi, J. Feng, S. Xiong, *Adv. Mater.* **2018**, 30, 1700104.
- [30] X. Qi, K. Huang, X. Wu, W. Zhao, H. Wang, Q. Zhuang, Z. Ju, *Carbon* **2018**, 131, 79.
- [31] S. Komaba, T. Hasegawa, M. Dahbi, K. Kubota, *Electrochem. Commun.* **2015**, 60, 172.